Polarization-dependent imaging contrast in abalone shells

Rebecca A. Metzler,[1] Dong Zhou,[1] Mike Abrecht,[2] Jau-Wern Chiou,[3] Jinghua Guo,[4] Daniel Ariosa,[5] Susan N. Coppersmith,[1] and P. U. P. A. Gilbert[1,*]

[1]*Department of Physics, University of Wisconsin, Madison, Wisconsin 53706, USA*
[2]*Synchrotron Radiation Center, 3731 Schneider Drive, Stoughton, Wisconsin 53589, USA*
[3]*Department of Applied Physics, National University of Kaohsiung, Kaohsiung 81148, Taiwan*
[4]*Advanced Light Source, Lawrence Berkeley National Laboratory, Berkeley, California 94720, USA*
[5]*Institute for the Physics of Complex Matter, EPF-Lausanne, Lausanne CH-1015, Switzerland*
(Received 4 August 2007; revised manuscript received 17 October 2007; published 19 February 2008)

Many biominerals contain micro- or nanocrystalline mineral components, organized accurately into architectures that confer the material with improved mechanical performance at the macroscopic scale. We present here an effect which enables us to observe the relative orientation of individual crystals at the submicron scale. We call it polarization-dependent imaging contrast (PIC), as it is an imaging development of the well-known x-ray linear dichroism. Most importantly, PIC is obtained *in situ*, in biominerals. We present here PIC in the prismatic and nacreous layers of *Haliotis rufescens* (red abalone), confirm it in geologic calcite and aragonite, and corroborate the experimental data with theoretical simulated spectra. PIC reveals different and unexpected aspects of nacre architecture that have inspired theoretical models for nacre formation.

PACS number(s): 61.05.cj, 87.85.J−

INTRODUCTION

Nacre, or mother-of-pearl, is intensely studied by materials scientists, mineralogists, physicists as well as chemists because of its remarkable mechanical properties and its fascinating and poorly understood formation.[1,2] Nacre is a composite of layered 400-nm-thick aragonite tablets[3] and 30-nm-thick organic matrix layers.[4,5] Aragonite, an orthorhombic $CaCO_3$ polymorph, is hard but brittle. Aragonite accounts for 95% of nacre's mass, leading one to expect the mechanical characteristics of nacre to be similar to those of aragonite, yet nacre is 3000 times more resistant to fracture than aragonite.[6] Materials scientists have only recently begun to learn how to prepare synthetic composites outperforming their components by such large factors.[7–11] However, the process necessary to produce such materials is complex and not as orderly in its organization as natural nacre.[11] It is, therefore, of extreme interest to understand and possibly harness the mechanisms of nacre formation. Here, we report observations on the structure and architecture of nacre enabled by the use of x-ray absorption near edge (XANES) spectroscopy,[12] combined with photoelectron emission spectromicroscopy (X-PEEM).[13] These observations inform and inspire other theoretical models for nacre formation mechanisms.[14]

We recently detected polarization-dependent imaging contrast (PIC) in X-PEEM images of red abalone (*Haliotis rufescens*) nacre.[14] Using X-PEEM, we observe that the intensities of two specific peaks, in the carbon and oxygen *K*-edge spectra, are anticorrelated. In the X-PEEM experiment, the spectral peak intensities correspond to imaging pixel intensities, therefore PIC appears in real-time, full-field images. When detected in spectroscopy alone, without imaging, this effect is commonly referred to as x-ray linear dichroism, and it has been observed in magnetic materials,[15,16] molecular chemisorbed systems,[17] and liquid crystals.[18] In carbonates, linearly polarized light provokes intense emission of specific

peaks depending on the orientation of the carbonate crystal *c*-axis relative to the polarization vector.[12,19] The linear polarization vector is always in the synchrotron orbit plane, and is therefore horizontal. If a complex biomineral containing multiple crystals is observed at once, the crystals with *c*-axes parallel or perpendicular to the polarization vector will appear white or black, respectively. Crystals with intermediate positions will appear with varying gray levels. This effect, widely studied in the man-made systems mentioned above, has been observed in naturally occurring minerals,[20,21] but has not been previously documented in a biomineral.

Here, we comprehensively present the observation of polarization-dependent contrast with XANES spectra from red abalone shells, including the nacreous and prismatic layers. The latter comprises columns of the trigonal-rhombohedral $CaCO_3$ polymorph calcite. We also present XANES spectra from aragonite and calcite crystals, and show that they exhibit x-ray linear dichroism similar to that observed in the biomineral. We compare the data from crystals with simulated spectra and find good agreement between experimental and theoretical trends.

Fully characterizing dichroism in calcite and aragonite enables us to study new aspects of biomineral structure *in situ*, in the solid, unthinned, and unstained biomineral. We show here a complete set of PIC images of the nacreous and prismatic layers in abalone shells at the submicron, micron, and millimeter scales. These results highlight the capabilities afforded by PIC.

METHODS

Our minimally destructive X-PEEM experiments probe a depth of ∼3 nm at the C *K*-edge (Fig. 1),[22] and can be done *in situ* in biominerals as discussed in detail by Gilbert *et al.*[23,24] The only requirement is a flat surface for X-PEEM spectromicroscopy analysis, which is easily obtained by polishing.
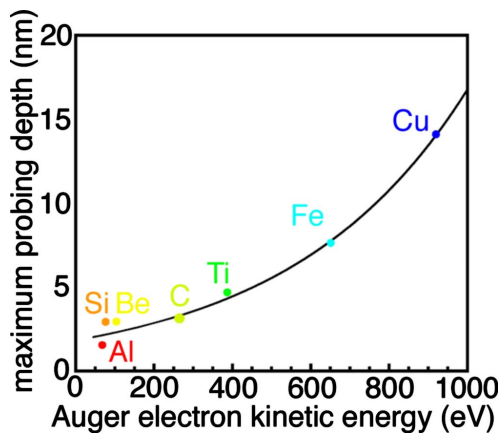
FIG. 1. (Color online) The escape depth of secondary photoelectrons at the C *K*-edge is ~3 nm, therefore only one layer of nacre tablets or prismatic crystals at a time is probed. The curve is an exponential fit to the experimental data points. Data adapted from Frazer *et al.* (Ref. 22).

We characterized PIC in red abalone by probing different regions within each shell, and multiple shells. Using the spectromicroscope for the photoelectron imaging of nanostructures with x rays (SPHINX) X-PEEM,[14] samples were analyzed after embedding and polishing at different angles. PIC in SPHINX images guides navigation on the sample surfaces, identification of the nacre and prismatic layers, and localization of the boundary between them.

The geometry of the microscope is described extensively elsewhere[13] and simplified for this paper in Fig. 2. The parameter most relevant to the current experiments is the angle between the polarization vector in the illuminating light, and the *c*-axis of each crystal or microcrystal. Soft x rays from either an undulator or bending magnet synchrotron source are always polarized linearly and horizontally, that is, in the synchrotron orbit plane. Depending on the orientation of each crystal, its *c*-axis forms a different angle with respect to the polarization vector. Here, this angle is called θ, or the polar angle. In the SPHINX setup, the beam illuminates the sample at a grazing incidence angle of 16°, and the sample is always mounted vertically. The polarization vector, therefore, is always at 16° from the sample normal.

A schematic of both the X-PEEM spectromicroscopy and the XANES spectroscopy experiments is presented in Fig. 2.

XANES spectra from geologic calcite and aragonite were acquired using two different chambers at two different synchrotrons: the XAB chamber at the SRC, installed on the HERMON beamline (80–1300 eV, spot size 300 $\times$ 1000 μm^2), and the AXIS chamber at the ALS on beamline 7.0.1 (80–1200 eV, spot size 500 $\times$ 500 μm^2). All of the C spectra for aragonite and calcite were acquired at ALS, all of the O spectra at SRC. In all cases, the sample surface was maintained vertical, and the measurement was done in total electron yield. The polar dependence was obtained by changing the polar angle θ for the two crystals. The aragonite and calcite crystals for C spectroscopy were polished so the *c*-axis was in plane. Polar variation was achieved by rotating the aragonite sample position azimuthally, around the normal
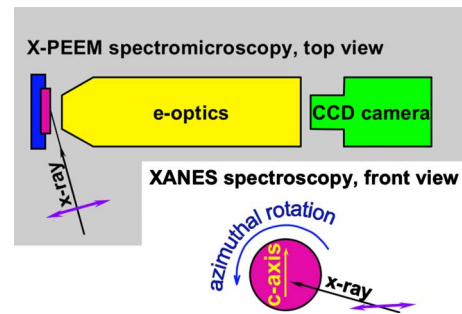

FIG. 2. (Color online) The geometry of the X-PEEM spectromicroscopy experiment at SRC in top view is reported on a gray background. Notice that the x rays illuminate the magenta sample at 16° grazing incidence and the electron optics axis is parallel to the sample normal. The geometry of the XANES experiment at the ALS is reported on a white background. In this case, we present a front view of the single-crystal sample, with its *c*-axis in plane, and the azimuthal rotation afforded by the manipulator. Notice that the x-ray beam illuminates the sample surface at normal incidence. In both experiments, the polarization is linear and horizontal (in the orbit plane), and represented by a purple vector.

to its surface, while illuminating it with linearly polarized light, as shown in Fig. 2. Similarly, the aragonite crystal for O spectroscopy had the *c*-axis in plane and was rotated azimuthally. The calcite crystal for O spectroscopy was cleaved so the *c*-axis was 40° from the sample surface normal. For calcite O spectroscopy, polar variation was obtained by rotating the sample around a vertical axis. In the polar dependence curves, the error bars are smaller for C than for O because the AXIS chamber is equipped with accurate azimuthal rotation on the sample manipulator, while the XAB chamber is not. For the latter, the sample had to be inaccurately rotated via a transfer rod, leading to inferior repeatability.

All single-crystal samples were cleaned three times in ultrasonic baths, with trichloroethane, acetone, and ethanol, respectively, for 20 min each, characterized and oriented with x-ray diffraction (PANalytical X'Pert PRO, Materials Science Center, UW-Madison), and repolished to remove the radiation-damaged surface. Before analysis, all samples, mineral and biomineral, were embedded in two-component epoxy resin (Buehler, Lake Bluff, IL), cured at room temperature for 24 h, and polished with decreasing size alumina grit (MasterPrep, also from Buheler) down to 0.05 μm, then cut to 1 cm^2 to fit the sample holder size. They were then coated with Pt to improve conductivity (1 nm Pt in the analyzed area, 50 nm around it).

RESULTS

In amorphous or unstructured samples, illumination with linearly polarized x-ray photons generates no contrast. In crystals, however, the intensity of specific peaks, associated with specific bonds, varies depending on the orientation of the polar angle. Because the prismatic and nacre layers of red abalone shells consist of calcite and aragonite microcrystals, variation in crystalline orientation relative to the soft-x-ray

TABLE I. Contrast ranges measured in different PIC maps. The contrast range is defined as the difference in mean gray levels between the brightest and the darkest tablets observed. The PIC maps yielding the greatest contrast are highlighted in boldface.

Map	Brightest tablet mean gray level	Darkest tablet mean gray level	Contrast range (brightest-darkest mean gray levels)
O map π^*/σ^*	179	72	107
O map π^*/pre-edge	**223**	**31**	**192**
C map π^*/σ^*	**233**	**138**	**108**
C map π^*/pre-edge	123	50	73

beam generates imaging contrast: the PIC discussed here.

In Fig. 3, we present the carbon, oxygen, and calcium maps and spectra from a nacre sample surface. The different gray levels in the carbon and oxygen maps of Fig. 3 correspond to variations in the intensity of the 290.3 eV peak and 534 eV peak, which are the C $1s \rightarrow \pi^*$ and O $1s \rightarrow \pi^*$ transitions of the carbonate CO bond (hereafter called the π^* peaks), and the 302 and 540 eV peaks associated with the C $1s \rightarrow \sigma^*$ and O $1s \rightarrow \sigma^*$ transitions of the carbonate CO bond (σ^* peaks). Immediately adjacent tablets exhibit strikingly strong contrast, as shown by the different gray levels, due to different c-axis orientations of adjacent crystalline tablets in each nacre layer. The π^* and σ^* peaks are anticorrelated and exhibit the PIC or linear dichroism described above. Mapping these peaks yields PIC, as shown in Fig. 3.

The carbonate C $1s \rightarrow \pi^*$ peak position varies from sample to sample between 290.2 and 290.4 eV. We, therefore, report it here as 290.3 ± 0.1 eV. This should be considered the uncertainty for all other energies reported hereafter.

In the raw data of the C and O PIC maps of Fig. 3, we observe different intensities for the brightest and darkest tablets, as reported in Table I.

As expected, in Table I we observe that the π^*/σ^* maps exhibit similar numeric values for the contrast in C and O maps (107 and 108, respectively), since C and O are bonded to each other in carbonates. It is also clear, however, that the contrast is greater for the π^*/σ^* map for C and for the π^*/pre-edge map for O (bold in Table I). For this reason, in Fig. 3 and all following figures from nacre and prismatic layers, we report these two maps.

An additional reason for selecting π^*/σ^* and π^*/pre-edge for C and O maps, respectively, is that they do not emphasize spots of organic material in the sample and therefore do not muddy the signal from mineral crystals. Mapping only highlights pixels in which the spectra have different intensities. As in organic molecules the intensities at 290.3 and 302 eV (the π^* and σ^* energy positions for carbonates) are very similar, organics do not map in π^*/σ^* C maps. Similarly, the intensities at 534 and 531 eV are similar in organic spectra, therefore organics are not mapped in π^*/pre-edge O maps.

Calcium does not exhibit the contrast observed in C and O maps. This is interesting in view of a previous report that Ca in CaF_2 exhibits polarization dependence. That observation was due to breaking of the cubic symmetry at the CaF_2 surface.[25] Our understanding is that PIC is bond specific rather than element specific. We interpret the lack of contrast

in nacre calcium maps as lack of preferential directionality of CaO bonds with respect to the polarization vector. Thus, Ca maps do not reveal individual tablets, and appear similar to images obtained with X-PEEM at energies away from π^* and σ^* peaks, or with any other microscopy technique.

The Ca spectra of Fig. 3 show that the nacre regions examined, as expected, are aragonitic. Calcite and aragonite spectra are most distinct at the Ca L-edge in the energy ranges indicated by boxes in Fig. 4. Peaks at these energies are assigned to crystal field resonance, which differs for different carbonates.[25–27] The calcite and aragonite spectra at the Ca L-edge are shown in Fig. 4.

In Fig. 5, we present X-PEEM data acquired on a cross section of a prismatic layer. The growth direction is at 90° from the polarization vector. PIC is also observed for C and O maps in Fig. 5, revealing more than ten calcitic prismatic crystals with the expected size and morphology. The Ca map, again, does not show dichroic contrast among carbonate crystals. It only shows low-calcium regions (dark) surrounding each calcite prism, as well as some splotches, which we interpret as organic material.

As mentioned, PIC is the origin of the contrast observed in nacre tablets and prismatic crystals in Figs. 3 and 5. To substantiate this observation, we extended the analysis to simpler systems: geologic aragonite and calcite single crystals, as reported in Figs. 6–8. We clearly see that varying the polar angle θ, the angle between the c-axis and polarization vector, dramatically changes the intensity of the π^* and σ^* peaks. Polar angle θ variation, therefore, is the origin of the contrast observed in Figs. 3 and 5. In those cases, the polarization vector and sample position were constant, while the orientation of adjacent crystallites varied. We report the unnormalized data in Fig. 7 because the effect of polar variation is already evident in these raw data. The most conventional and accepted data presentation, however, is that of normalized data, as shown in Figs. 3–6 and 8.

PIC must arise from variations of the polar angle θ because the relative intensities of the peaks cannot vary when only the ab-plane angle is rotated around the c-axis,[12] since the orientations of carbonate planar triangles in aragonite and calcite have hexagonal symmetry in the ab-plane.[28] Visualizing each carbonate group as a triangle, along one carbonate plane (ab-plane) all triangles are repeated identically. In the next carbonate plane, however, the triangles are rotated, so that two overlapping triangles form a "star of David" shape.

The least manipulated data presentation for the polar dependence of C spectra is that used in Figs. 6(e) and 8(e),
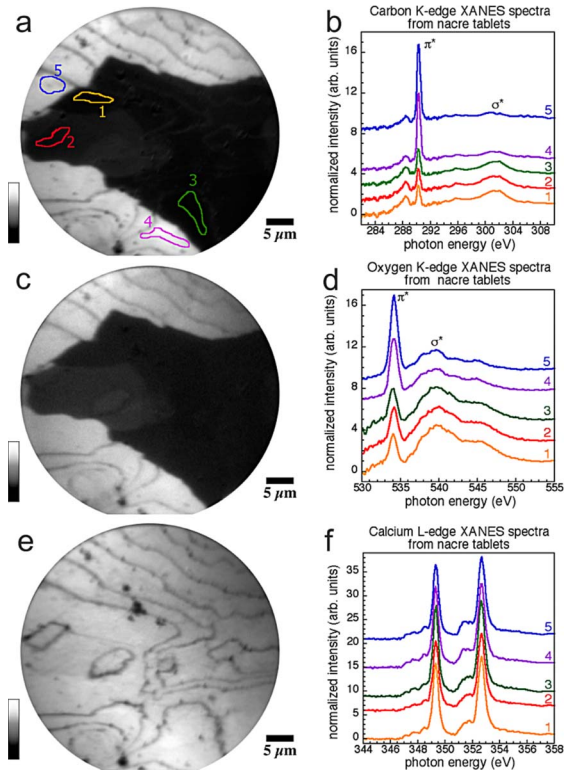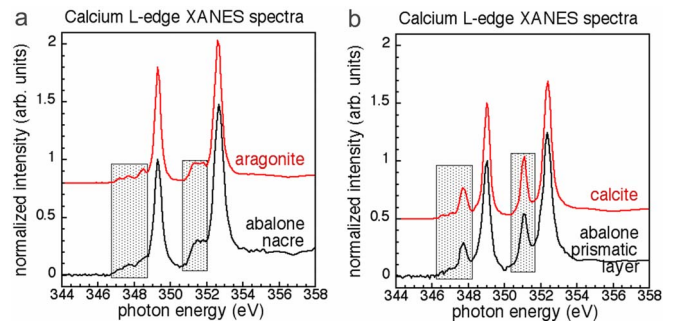
FIG. 4. (Color online) (a) Aragonite and (b) calcite Ca *L*-edge XANES spectra acquired on geologic aragonite and calcite crystals (red curves). These spectra are dramatically different in the crystal field resonance regions highlighted by the gray boxes. They are, however, very similar to the spectra of nacre and prismatic crystals, respectively (black curves).
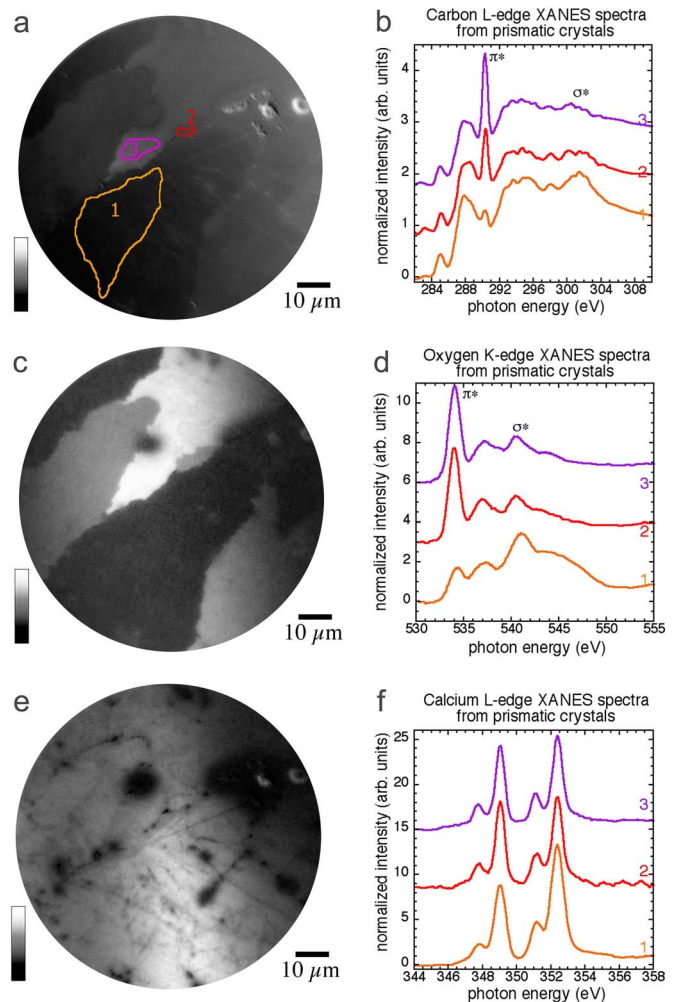

FIG. 3. (Color online) (a) Carbon π^*/σ^* map of the polished surface of red abalone nacre, showing polarization-dependent imaging contrast (PIC). The map was obtained by digital ratio of two SPHINX micrographs, acquired at 290.3 and 302 eV, respectively, the π^* and σ^* peak energies shown in (b). The immediately adjacent tablets labeled 1 and 5 exhibit the highest contrast. Different gray levels correspond to different crystal orientations. (b) Carbon spectra extracted from the correspondingly labeled regions in (a). The intensities of the π^* and σ^* peaks are anticorrelated and vary dramatically from tablet to tablet, generating the contrast seen in (a), which in turn depends on crystal orientation and polarization. These and all other C spectra were normalized to a beamline background, and then to a linear fit above 310 eV, so that the spectral intensities below 283 eV and above 310 eV are 0 and 1, respectively. (c) Oxygen map obtained by digital ratio of images at 534 and 531.7 eV, the π^* and pre-edge energies, respectively. (d) Oxygen spectra from the same regions, reproducing the anticorrelation of the π^* and σ^* peaks seen for carbon. All O spectra were normalized to a beamline background, and then to a linear fit above 555 eV so that spectral intensities below 530 eV and above 555 eV are 0 and 1, respectively. (e) Calcium map of the same nacre area, obtained by digital ratio of images at 352.7 and 343.7 eV. This map represents only a distribution map, showing much greater Ca concentration in the tablets compared to the organic matrix layers separating them. The polarization dependence observed in (a) and (c) is not detected in this map. (f) Calcium spectra extracted from the regions labeled in (a), showing that all regions examined are aragonite. All Ca spectra were normalized to a linear background, representative of the beamline background, and then to a linear fit above 355 eV so that spectral intensities below 346 eV and above 355 eV are 0 and 1, respectively. The nacre growth direction of this sample is perpendicular to the sample surface, therefore the organic matrix layers are parallel to the sample surface. As they are not perfectly flat, they appear as contour lines.

FIG. 5. (Color online) (a) Carbon π^*/σ^* map from the surface of a polished cross section of red abalone prismatic layer. (b) Carbon *K*-edge XANES spectra extracted from the correspondingly labeled regions in (a) exhibit anticorrelated intensity of the π^* and σ^* peaks. (c) Oxygen map of the π^*/pre-edge signal at 534 and 528 eV, respectively. (d) Oxygen *K*-edge XANES spectra. (e) Calcium distribution map of the same prismatic region, obtained by a digital ratio of images acquired at 351.4 eV (on the calcite peak) and 344.4 eV. (f) Calcium *L*-edge XANES spectra extracted from regions labeled in (a), showing that all regions examined are calcite.
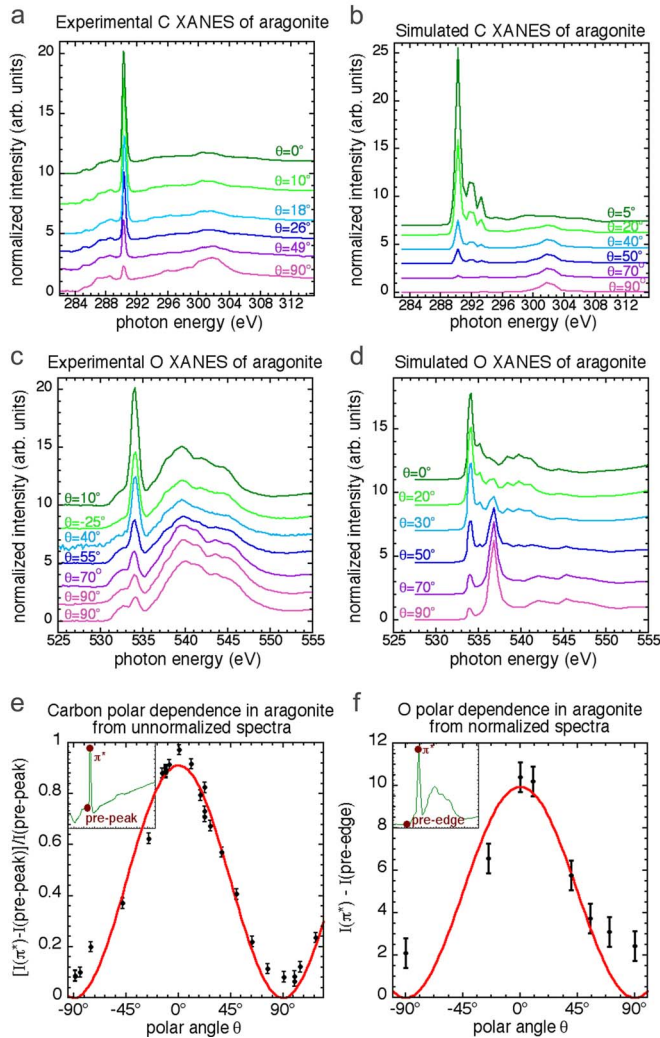
FIG. 7. (Color online) Selected raw data XANES spectra acquired at different polar angles. Even in these raw data the decrease of π^* peak intensity with θ is evident. Again, only selected spectra are shown for clarity. The only processing here was vertical displacement and scaling, necessary because the spectra had wide variations in intensity. The black curve, labeled I_o, is the beamline background curve, acquired simultaneously with the $\theta=0$ spectrum. Each of the spectra in Fig. 6(a) was normalized to a different I_o, simultaneously acquired. The polar variation of Fig. 6(e) was obtained from these and many other spectra.

obtained directly from unnormalized raw spectra as those of Fig. 7 and by simply measuring the on-peak and off-peak intensities, $I(\pi^*)$ and I(pre-peak). For the off-peak intensity, we selected the immediate pre-peak at 289.5 eV. Since in the unnormalized raw data (e.g., Fig. 7) the spectral intensity varies dramatically, we measured the numeric values of $I(\pi^*)$ and I(pre-peak) in each unnormalized spectrum and report $[I(\pi^*)-I(\text{pre-peak})]/I(\text{pre-peak})$ in Figs. 6(e) and 8(e).

For the oxygen spectra, the π^* peak is directly on the background, and not above the absorption edge as in C. Normalized or unnormalized spectra can, therefore, be used, and the off-peak energy is simply the pre-edge energy. In Figs. 6(f) and 8(f), we report $I(\pi^*)-I(\text{pre-edge})$ from normalized spectra, as shown in the inset.

The experimental data of Figs. 6–8 clearly reveal the polar dependence at the origin of the PIC effect. The polar dependence has a maximum at $\theta=0°$ and minima at $\pm90°$. A $\cos^2\theta$ dependence was predicted by theory and observed in chemisorbed carbonate groups with XANES spectroscopy by Stöhr's and co-workers.[12,19]

A detailed discussion of the peak observed at 285 eV is reported below in the Appendix.

Simulations of the aragonite and calcite XANES spectra were done using the FEFF 8.2 software package,[29] with an input file that used crystal coordinates for aragonite and calcite[28,30] and the POLARIZATION card to vary the polar angle θ. Both the experimental and simulated spectra exhibit increase and decrease in the π^* and σ^* peak intensities, respectively, as the polar angle is decreased. Despite the lineshape inaccuracy of the simulated spectra, the anticorrelation of π^* and σ^* peaks is in good agreement with the experimental data.

Having characterized the PIC effect in aragonite and calcite, we now use it to analyze the structure of nacre and prismatic crystals in red abalone nondestructively, by prob-

FIG. 6. (Color online) (a) Carbon spectra acquired from a single geologic aragonite crystal as the polar angle θ was varied. Only a subset of the spectra was displayed and offset for clarity. (b) FEFF simulated C spectra for aragonite at different polar angles. While the lineshape does not accurately portray the experimental data, the anticorrelation between the π^* and σ^* peaks is consistent in the experimental and simulated spectra. (c) Oxygen spectra from another single crystal of aragonite. (d) FEFF simulated O spectra. (e) Polar dependence (black dots) of the π^* peak, obtained by measuring, in the raw data of Fig. 7 and others, the intensities at 290.3 and 289.5 eV. These are the π^* peak and the immediate pre-peak intensity, respectively, shown in the inset. Due to intensity variations in the unnormalized data, each of the π^* peak intensities had to be scaled to its pre-peak intensity. The parameter displayed, therefore, is not $I(\pi^*)-I(\text{pre-peak})$ but $[I(\pi^*)-I(\text{pre-peak})]/I(\text{pre-peak})$. A direct measurement of the error bars was obtained from three repeated acquisitions returning to $\theta=-11°$ and $\theta=22°$. Theory predicts a variation of the π^* intensity with a $\cos^2\theta$ dependence (Refs. 14 and 15). A fit of the experimental data (red curve) reveals that the dependence is indeed $[I(\pi^*)-I(\text{pre-peak})]/I(\text{pre-peak})=\alpha\cos^2\theta$. The fit parameter α is 0.9 for carbon in aragonite. (f) The polar dependence for the normalized oxygen spectra in (c), and $I(\pi^*)-I(\text{pre-edge})=\alpha\cos^2\theta$ fit (red curve), with $\alpha=10$ for O in aragonite.
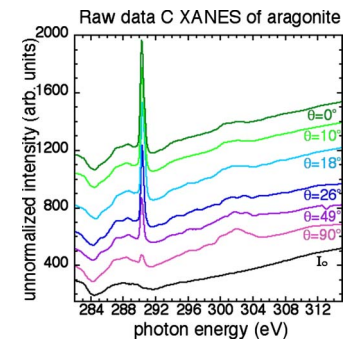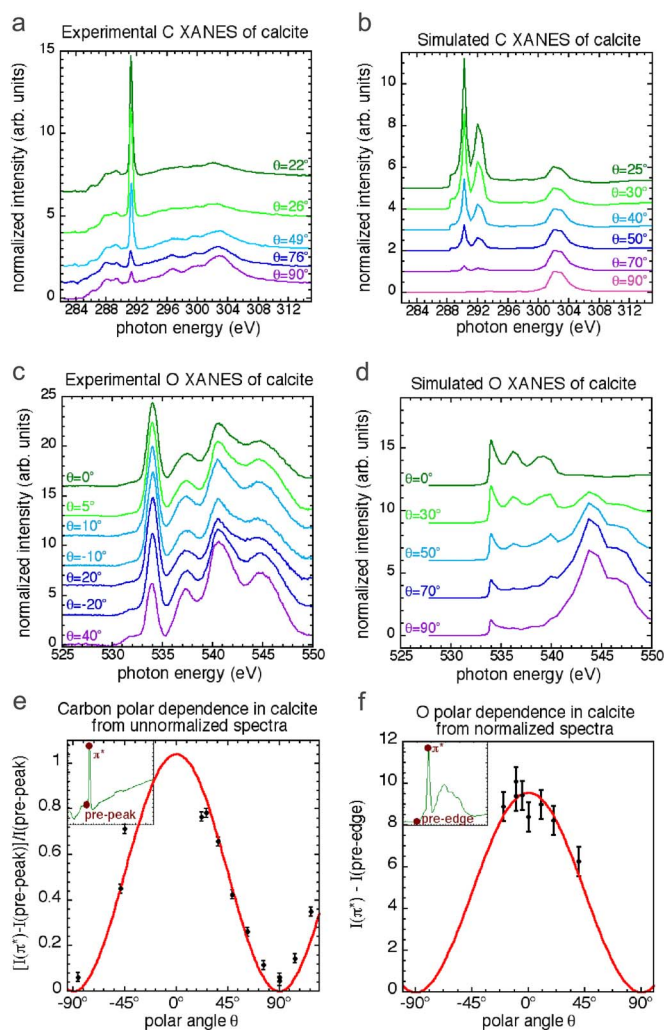
FIG. 8. (Color online) (a) Carbon spectra of a single crystal of geologic calcite at different polar angles. (b) FEFF simulated carbon spectra of calcite. Oxygen (c) experimental and (d) simulated spectra. (e) Carbon and (f) oxygen polar dependence data (black dots) and fit (red curves). Again, the two data points at $\theta=90°$ for C and $\theta=-10°$ for O indicate the experimental uncertainty. As in Fig. 6, we report $[I(\pi^*)-I(\text{pre-peak})]/I(\text{pre-peak})$ for C and $[I(\pi^*)-I(\text{pre-edge})]$ for O spectra. As for aragonite, also for calcite an acceptable fit is obtained by $\alpha\cos^2\theta$ with $\alpha=1$ for carbon and $\alpha=10$ for oxygen.

ing the relative crystallographic orientation of nacre tablets and prismatic crystals from the submicron to the millimeter scale.

In principle, the polar dependence curves presented at the end of Figs. 6 and 8 could be used as calibration curves to assign crystallographic orientation to the individual nacre tablets and prismatic crystals. Thus far, the maximum carbon $[I(\pi^*)-I(\text{pre-peak})]/I(\text{pre-peak})$ found in nacre is 0.88, which is well within the range observed for aragonite: up to 0.97. For prismatic crystals, the maximum carbon $[I(\pi^*)-I(\text{pre-peak})]/I(\text{pre-peak})$ measured was 0.48, which is well below the calcite maximum of 0.78, even without having reached the maximum at $\theta=0°$. However, further work is required to make PIC a rigorously quantitative measurement.
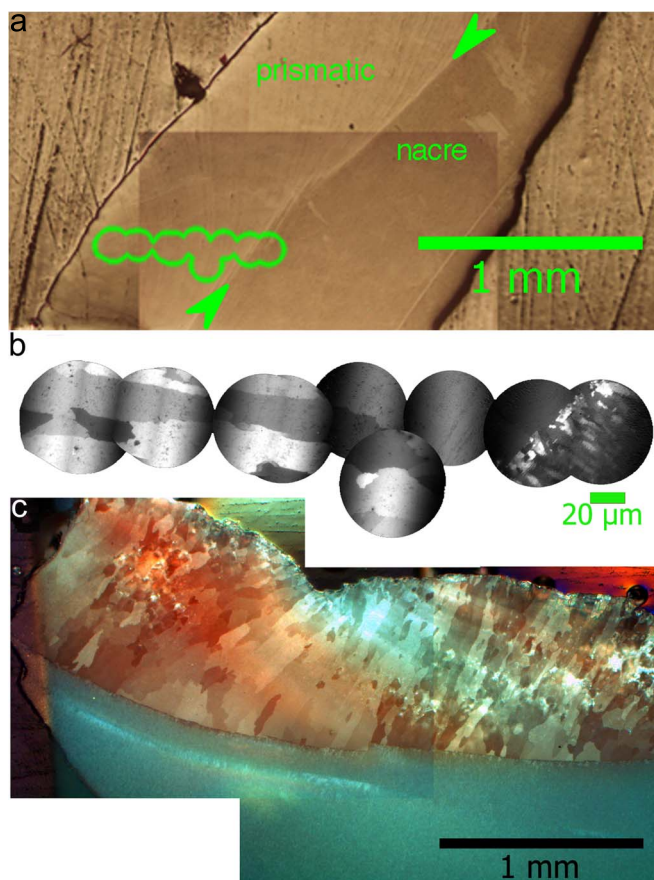

FIG. 9. (Color online) (a) Composite VLM images of a polished cross section of red abalone, acquired in differential interference contrast mode. The green circles indicate prismatic areas examined with SPHINX. (b) A series of π^*/pre-edge O maps of the areas shown in (a). (c) VLM image taken with crossed polarizers on the same red abalone shell. The prismatic crystals appear on top in various shades of brown, the nacre is cyan, at the bottom.

In practice, a calibration curve must be obtained from nacre and prismatic layers directly. This will verify if there are differences in the π^* peak intensities in biogenic minerals versus geologic crystals. A comparison of nacre and aragonite calibration curves may reveal differences due to the presence of organics, or the small lattice distortions observed by Pokroy *et al.*[31] Accurate calibration curves similar to those presented here must be obtained from single nacre tablets and prismatic crystals to enable this quantitative analysis. Such data are extremely challenging to obtain, and will be the subject of a future paper.

The visible light microscopy (VLM) image of Fig. 9 shows the cross section of the red abalone shell, including the prismatic and nacre layers, and the boundary between the two. O maps were acquired over a distance of 400 μm in the prismatic region by taking multiple partly overlapping PIC images [Fig. 9(b)]. Comparable contrast was obtained, showing that the same distribution of angular orientations persists independent of distance from the nacre-prismatic boundary. Due to the large crystal size, individual crystals and their orientation can be seen in VLM using two crossed polarizer filters, one in the analysis channel and one in the illumination
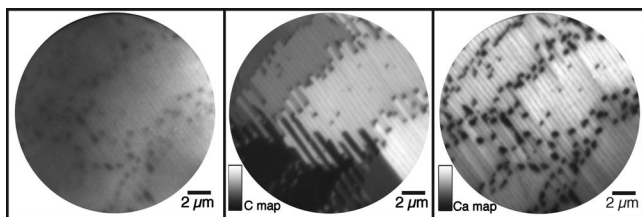
FIG. 10. Single-energy SPHINX image at 344 eV, carbon and calcium maps, taken near a growth layer in polished red abalone nacre. The carbon π^*/σ^* map is the ratio of two images taken at 290.3 and 302 eV, respectively, and the calcium map is the ratio of 352 and 344 eV images. In this 90° cross section, the growth direction was in plane, at 74° from the polarization vector. Notice the PIC imaging contrast in the carbon map, while the direct image and the Ca map do not show any contrast. Dark Ca-poor spots in the Ca map appear at the sides of each tablet, where organics were located.

channel [Fig. 9(c)]. Images acquired with the VLM also show different crystal orientations in the prismatic layer, consistent with the PIC observed in X-PEEM images. In the nacre layer, however, the tablet crystals are too small and too transparent to be seen in cross-polarized VLM.

The C and Ca maps in Fig. 10 show a high-resolution image of nacre tablets in cross section. As seen previously, the C map shows PIC due to polar disorder in nacre tablets, while the Ca map does not show any dependence on crystal orientation. This high-contrast area was a few microns away from one of the nacre growth layers.[32] The PIC gray level homogeneity within each tablet is consistent with previous reports that each tablet diffracts as a single crystal.[33]

In Fig. 11, we present a series of O maps acquired with SPHINX at and away from the nacre-prismatic boundary, across the whole thickness of the nacre layer. Our data dem-
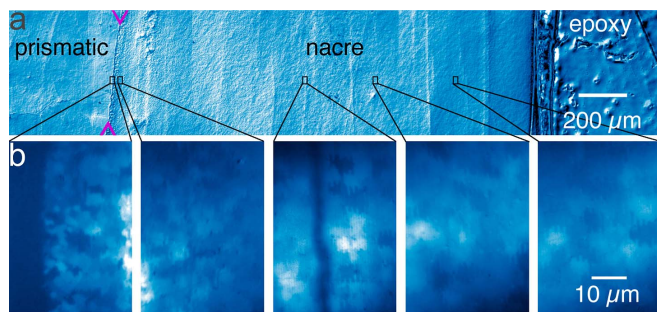

FIG. 11. (Color online) (a) Visible light microscopy composite micrographs of a polished section of red abalone shell, acquired in differential interference contrast mode. The nacre growth direction was 30° from the sample surface normal. The line between two magenta arrowheads is the prismatic-nacre boundary. The black rectangles outline the areas in which the O maps in (b) were acquired with SPHINX. (b) Series of oxygen PIC maps, obtained by digital ratio of images acquired at 534 and 530 eV, π^* and pre-edge, respectively. PIC is clearly detectable across the entire thickness of the nacre layer. The central PIC map was acquired across one of the vertical lines evident in the optical image, which do not appear to affect tablet order or contrast. To enhance contrast in bulk nacre, all raw grayscale maps were leveled and converted to a blue quadtone.
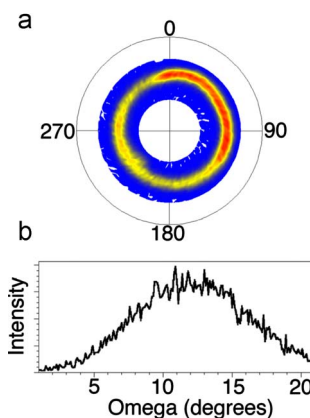

FIG. 12. (Color online) (a) X-ray diffraction pole figure indicates random orientation of nacre tablets in the ab-plane. (b) Rocking curve taken on the (002) Bragg peak on a piece of red abalone nacre. The 22° footprint of the rocking curve indicates that the c axis variation in bulk nacre varies by $\pm 11°$, with instrument resolution better than 0.1°.

onstrate conclusively that columns of tablets co-oriented with respect to their c-axes start and end over an unexpectedly short length scale. Similar short nacre columns had previously been identified, but only in terms of co-orientation of crystal axes within the ab-plane.[34] Here, thanks to the PIC in this figure, we observe that columns with several co-oriented tablets appear across nacre. The contrast observed in these maps is due to misorientation of the c-axes with respect to the polarization vector. Compared with the growth direction as well, the orientations of tablet c-axes differ from column to column. Our data, therefore, confirm that it is incorrect to identify the growth direction of nacre with the c-axis, as is commonly done in the literature.

From the SPHINX results of Fig. 11 and many others, we see that the largest PIC occurs near the nacre-prismatic boundary. The contrast, corresponding to the degree of c-axis crystallographic disorder, quickly diminishes with the distance from the boundary. This is in agreement with previous observations by DiMasi and Sarikaya, using synchrotron x-ray microdiffraction, that nacre tablets in red abalone are less co-oriented near the nacre-prismatic boundary and become more co-oriented and ordered within 100 μm of the boundary.[34] This also agrees with the bulk x-ray diffration measurements taken by our group and others,[33,35] which find that the a- and b-axes are randomly oriented, while the c-axes of nacre tablets deviate from the growth direction by only $\pm 11°$. This is the footprint of the rocking curve, reported in Fig. 12. We find that the maximum c-axis misorientation and PIC contrast are near the nacre-prismatic boundary, with a few exceptions. Occasionally, isolated regions away from the boundary exhibit extreme PIC. The data of Fig. 3 were acquired in one such region. Lesser but still distinct PIC, however, is observed across the whole 2 mm thickness of the nacre layer, as seen in Fig. 11.

DISCUSSION

We reported an extensive characterization of the PIC effect and its origin in the polarization-dependent spectral in-

tensities in the nacreous and prismatic layers of red abalone, as well as single crystals of geologic aragonite and calcite. Theoretical simulations of the single-crystal spectra are in good agreement with the experimental data. Combined, they fully explain the source of the contrast observed in red abalone shells.

It is interesting to notice that the values found for α the maximum polar dependence value at $\theta=0°$, for aragonite are 0.9 and 10 for C and O, and for calcite they are 1 and 10 for C and O, respectively. In each mineral, the difference between the C and O α values is not surprising. First of all, the absorption cross sections for C and O are different; second, the peak intensities measured are not the same. Due to the energy position of the π^* peak, which is above the C K-edge, and to the nonflat I_o at the C energies, the most accurate peak height is obtained by subtracting an immediate pre-edge value, as shown in the insets of Figs. 6 and 8. For O spectra, instead, the I_o is flat and the π^* is the lowest energy peak of the spectrum. This leads to greater π^* and α values for O than for C, in both aragonite and calcite.

The reproducibility of the π^* and α values for C in aragonite and calcite (0.9 and 1), and those for O (10 and 10), is an important validation. This result is consistent with the fact that the carbonate groups are very similar in the structures of aragonite and calcite;[28,30] therefore, the CO bonds they form, which are detected by XANES spectroscopy, are also similar.

In this work, we have initiated the use of PIC to study the nacreous and prismatic layers in red abalone. PIC only varies for different orientations of the c-axis in calcite, aragonite, or biogenic crystals. It does not vary for rotations in the ab-plane. We have confirmed that there is greater variation in the nacre tablet orientation near the nacre-prismatic boundary. We have discovered that columns of tablets with co-oriented c-axes appear in different gray levels, depending on tablet crystal orientation, and immediately adjacent columns may have completely different c-axis orientations. These columns of co-oriented tablets start and end abruptly. A possible explanation for this architecture relies on a specific formation mechanism for nacre, as described by Metzler *et al.*[14] In that simple static model, nucleation sites are randomly distributed on preexisting organic matrix layers, and co-orientation of tablets $n+1$ and $n+2$ is only possible if a nucleation site happens to be present between the two. A more sophisticated dynamic growth model is currently being developed. This will reveal which parameters are necessary

and which ones are auxiliary to the formation of nacre in its specific architecture unraveled by PIC.

With the full body of data presented here as its solid foundation, the PIC contrast mechanism can be used to investigate the structure and orientation of other polycrystalline systems and biominerals in particular, therefore revealing additional and exciting architectures in pristine biominerals, and possibly inspire and inform other mechanisms for the formation of complex biominerals.

APPENDIX

Detailed discussion of reference spectra

The aragonite cleaning procedure should have removed all adsorbed oils, humic substances, and other contaminants frequently present in geologic carbonates. In practice, however, they were not sufficient to remove all contaminants, as shown by the presence of residual C peaks around 285 eV, typical of aromatic organic molecules. These peaks are not the result of radiation damage, and their intensity decreases with sample cleaning. The contaminant peaks at 285 eV do not overlap any of the carbonate peaks, therefore their presence does not affect any observation of the carbonate peaks discussed below. Interestingly, these peaks appear in geologic aragonite but not in calcite, at least in the crystals studied here. In spectra from abalone shells, they do not appear in the aragonitic nacre and do appear in the calcitic prismatic layer. Data in nacre and prismatic layers were also acquired at doses far below the onset of damage. Therefore, this result may indicate differences in the proteins present in these two biominerals, with greater concentration of C═C double bonds in the prismatic layer than in the nacre layer.

*Previously publishing as Gelsomina De Stasio. Corresponding author; pupa@physics.wisc.edu

[1] H. A. Lowenstam and S. Weiner, *On Biomineralization* (Oxford University Press, Oxford, 1989).

[2] L. Addadi, D. Joester, F. Nudelman, and S. Weiner, Chem.-Eur. J. **12**, 980 (2006).

[3] S. Mann, *Biomineralization* (Oxford University Press, New York, 2001).

[4] I. M. Weiss, C. Renner, M. G. Strigl, and M. Fritz, Chem. Mater.

14, 3252 (2002).

[5] M. Rousseau, E. Lopez, P. Stempflé, M. Brendlé, L. Franke, A. Guette, R. Naslai, and X. Bourrat, Biomaterials **26**, 6254 (2005).

[6] J. D. Currey, Proc. R. Soc. London, Ser. B **196**, 443 (1977).

[7] Z. Tang, N. A. Kotov, S. Magonov, and B. Ozturk, Nat. Mater. **2**, 413 (2003).

[8] G. F. Xu, N. Yao, I. A. Aksay, and J. T. Groves, J. Am. Chem. Soc. **120**, 11977 (1998).

[9] H. Wei, N. Ma, F. Shi, Z. Wang, and X. Zhang, Chem. Mater. **19**, 1974 (2007).

[10] X. Y. Liu and S. W. Lim, J. Am. Chem. Soc. **125**, 888 (2003).

[11] A. Sellinger, P. M. Weiss, A. Nguyen, Y. Lu, R. A. Assink, W. Gong, and C. J. Brinker, Nature (London) **394**, 256 (1998).

[12] J. Stöhr, *NEXAFS Spectroscopy* (Springer-Verlag, Berlin, 1992).

[13] B. H. Frazer, M. Girasole, L. M. Wiese, T. Franz, and G. De Stasio, Ultramicroscopy **99**, 87 (2004).

[14] R. A. Metzler, M. Abrecht, R. M. Olabisi, D. Ariosa, C. J. Johnson, B. H. Frazer, S. N. Coppersmith, and P. U. P. A. Gilbert, Phys. Rev. Lett. **98**, 268102 (2007).

[15] Ch. Roth, F. U. Hillebrecht, H. Rose, and E. Kisker, Phys. Rev. Lett. **70**, 3479 (1993).

[16] J. Stöhr, A. Scholl, T. J. Regan, S. Anders, J. Lüning, M. R. Scheinfein, H. A. Padmore, and R. L. White, Phys. Rev. Lett. **83**, 1862 (1999).

[17] J. Stöhr, K. Baberschke, R. Jaeger, R. Treichler, and S. Brennan, Phys. Rev. Lett. **47**, 381 (1981).

[18] J. Stöhr, M. G. Samant, J. Lüning, A. C. Callegari, P. Chaudhari, J. P. Doyle, J. A. Lacey, S. A. Lien, S. Purushothaman, and J. L. Speidell, Science **292**, 2299 (2001).

[19] R. J. Madix, J. L. Solomon, and J. Stohr, Surf. Sci. **197**, L253 (1988).

[20] P. A. van Aken and S. Lauterbach, Phys. Chem. Miner. **30**, 469 (2003).

[21] D. H. Templeton and L. K. Templeton, Acta Crystallogr., Sect. A: Found. Crystallogr. **A53**, 352 (1997).

[22] B. H. Frazer, B. Gilbert, B. R. Sonderegger, and G. De Stasio, Surf. Sci. **537**, 161 (2003).

[23] P. U. P. A. Gilbert, B. H. Frazer, and M. Abrecht, in *Molecular Geomicrobiology*, edited by J. F. Banfield, K. H. Nealson, and J. Cervini-Silva (Mineralogical Society of America, Washington, DC, 2005), Vol. 59, pp. 157–185.

[24] G. De Stasio, B. H. Frazer, B. Gilbert, K. L. Richter, and J. W. Valley, Ultramicroscopy **98**, 57 (2003).

[25] D. Rieger, F. J. Himpsel, U. O. Karlsson, F. R. McFeely, J. F. Morar, and J. A. Yarmoff, Phys. Rev. B **34**, 7295 (1986).

[26] S. J. Naftel, T. K. Sham, Y. M. Yiu, and B. W. Yates, J. Synchrotron Radiat. **8**, 255 (2001).

[27] K. Benzerara, T. H. Yoon, T. Tyliszczak, B. Constantz, A. M. Spormann, and G. E. Brown, Jr., Geobiology **2**, 249 (2004).

[28] D. J. M. Bevan, Elisabeth Rossmanith, Darren K. Mylrea, Sharon E. Ness, Max R. Taylor, and Chris Cuff, Acta Crystallogr., Sect. B: Struct. Sci. **B58**, 448 (2002).

[29] A. L. Ankudinov, C. E. Bouldin, J. J. Rehr, J. Sims, and H. Hung, Phys. Rev. B **65**, 104107 (2002).

[30] E. Effenberger, K. Mereiter, and J. Zemann, Z. Kristallogr. **156**, 233 (1981).

[31] B. Pokroy, J. P. Quintana, E. N. Caspi, A. Berner, and E. Zolotoyabko, Nat. Mater. **3**, 900 (2004).

[32] X. Su, A. M. Belcher, C. M. Zaremba, D. E. Morse, G. D. Stucky, and A. H. Heuer, Chem. Mater. **14**, 3106 (2004).

[33] S. W. Wise, Eclogae Geol. Helv **63**, 775 (1970); Science **167**, 1486 (1970).

[34] E. DiMasi and M. J. Sarikaya, Mater. Res. **19**, 1471 (2004).

[35] C. M. Zaremba, A. M. Belcher, M. Fritz, Y. Li, S. Mann, P. K. Hansma, D. E. Morse, J. S. Speck, and G. D. Stucky, Chem. Mater. **8**, 679 (1996).